VOL. 81, NO. 14 JOURNAL OF GEOPHYSICAL RESEARCH MAY 10, 1976

EARTH TIDE STRAIN MEASUREMENTS IN THE POORMAN MINE NEAR BOULDER, COLORADO

J. Levine[1]

Time and Frequency Division, National Bureau of Standards, Boulder, Colorado 80309

J. C. Harrison

Cooperative Institute for Research in Environmental Sciences,
University of Colorado/National Oceanic and Atmospheric Administration,
Boulder, Colorado 80309

Abstract. Earth tide strains at a particular site are affected by the internal structure of the solid earth, ocean loads, local inhomogeneities in elastic constants due to geologic structure, topography near the observation site, and the cavity in which the measuring instrument is situated. All of these influences have been estimated quantitatively for the Poorman site for a diurnal (O_1) and a semidiurnal (M_2) tide. The predicted strains agree with those observed to within 5% for M_2 and 10% for O_1 whereas without the topographic and geologic corrections there is an amplitude discrepancy of about 25%. The phase discrepancy is reduced from -15° to -6° for O_1. The residuals can be reduced further by using terms quadratic in the applied potential, which may imply a breakdown of linear tide theory, a deficiency in classical tidal calculations, or a local effect that modulates the tidal transfer function of our site.

Although the general features of strain tides are well understood, a quantitative comparison between theory and experiment has never, to our knowledge, yielded the sort of agreement obtained for gravity tides.

In this paper we show that by considering local topography and local inhomogeneities in the elastic constant, much of the discrepancy between classical tide theory and observations can be removed, at least for the M_2 and O_1 components. Although we have not analyzed the other minor tidal components, we are confident that the same sort of agreement would result from such an analysis.

The Calculations

Harrison [1976] has pointed out that the strains induced in the earth by a large-scale stress field can be significantly modified at a given point by local topography and local inhomogeneities in the elastic constants. He shows that these modifications are only significant close to the topographic and geologic inhomogeneities and that corrections for these effects can be made by using finite element techniques. In order to keep these calculations to a manageable size, it is necessary to proceed by a series of scale arguments in which the irregularities are supposed to be of small scale compared with the stresses producing the deformation.

The largest scale tidal deformation is the body tide. As the gross properties of the earth are well represented by the Gutenberg-Bullen model, we have used the Love numbers computed for this model by Farrell [1972a] and expect the results to be representative when they are averaged over an area large compared with the topographic and geologic irregularities. Similarly, the gross strains produced near Boulder by the ocean tide loads may be calculated by using the same earth model; accordingly, we have used Farrell's [1972a] Green's functions for this model. The M_2 tide convolution was done by Farrell [1972b] and utilizes Hendershott's ocean tide model [Hendershott and Munk, 1970], modified along the California coast according to the study by Munk et al. [1970]. The ocean tide model of Tiron et al. [1967] was used at the O_1 frequency.

These gross strains may be expected to suffer local modification by geologic and topographic inhomogeneities in the vicinity of the observation site. The geologic sketch map (Figure 1) shows the Poorman Mine to be located in a Precambrian granite batholith (Boulder Creek batholith). Although this granite is complexly faulted and mineralized, particularly near the Poorman Mine [Humphrey, 1955], the mineralized zones are quite thin and the faults inactive. We have made no attempt to model these inhomogeneities and have treated the entire Precambrian basement as a homogeneous mass with elastic properties appropriate for granite. The map, however, shows the Poorman Mine to be located near a major geologic discontinuity between Precambrian igneous and metamorphic basement rocks to the west and Phanerozoic sediments to the east. The transition is exceedingly abrupt; the sediments are about 3700 m thick very close to the boundary, and they extend eastward from the boundary with only gradual changes in thickness for over 1500 km. The Poorman Mine lies about two thirds of the sediment thickness to the west of this major discontinuity, which may therefore be expected to

---

[1] Also at Joint Institute for Laboratory Astrophysics of the National Bureau of Standards and University of Colorado, Boulder, Colorado 80309 and at Department of Physics and Astrophysics, University of Colorado, Boulder, Colorado 80309.

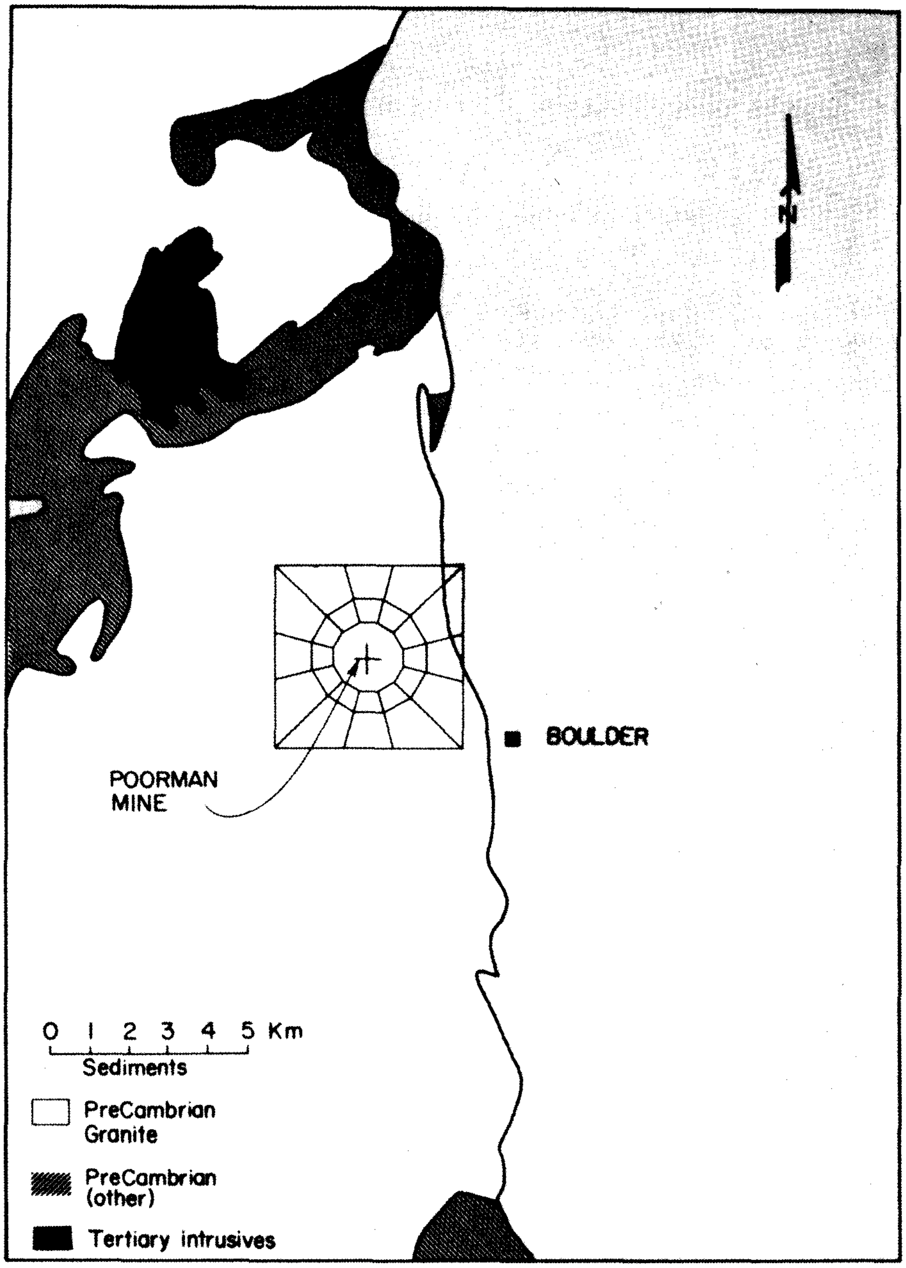

Fig. 1. Geologic sketch map of the vicinity of the Poorman Mine. Part of the finite element grid used in three-dimensional topographic calculation is also shown.

modify the tidal strain at the mine significantly.

A two-dimensional finite element calculation was used to estimate the influence of this discontinuity. The granite was modeled with Young's modulus equal to 7.5 times 10^{11} dyn/cm^2 and Poisson's ratio equal to 0.25 (V_p = 5.8 km/s; V_s = 3.35 km/s, if the density is 2.67 g/cm^3). The sediments range in age from Cambrian to Tertiary and are variable in lithology and seismic velocity. The velocity log from the Rocky Mountain arsenal well in Denver [Healy et al., 1966] yields a mean P wave velocity of 3.5 km/s through the section. The S wave velocities have not to our knowledge been determined for this section. Erickson et al. [1968], summarizing work (elsewhere) with continuous signal S wave sources, conclude, 'In the deeper sedimentary section, the shear wave velocity averages about one half the corresponding P-wave velocity....' Accordingly, we have used values of Young's modulus and Poisson's ratio of 2.08 × 10^{11} dyn/cm^2 and 0.33, which correspond to P and S wave velocities of 3.6 and 1.8 km/s for a density of 2.4 g/cm^3. These values are probably too high for the upper half of the section and too low for the lower half; fortunately, our final results are rather insensitive to these assumptions because the Poorman strainmeter is almost parallel to the Precambrian-sediment boundary.

The model is shown in Figure 2, which is reproduced from Harrison [1976]. The Precambrian sediment boundary was assumed to be straight with

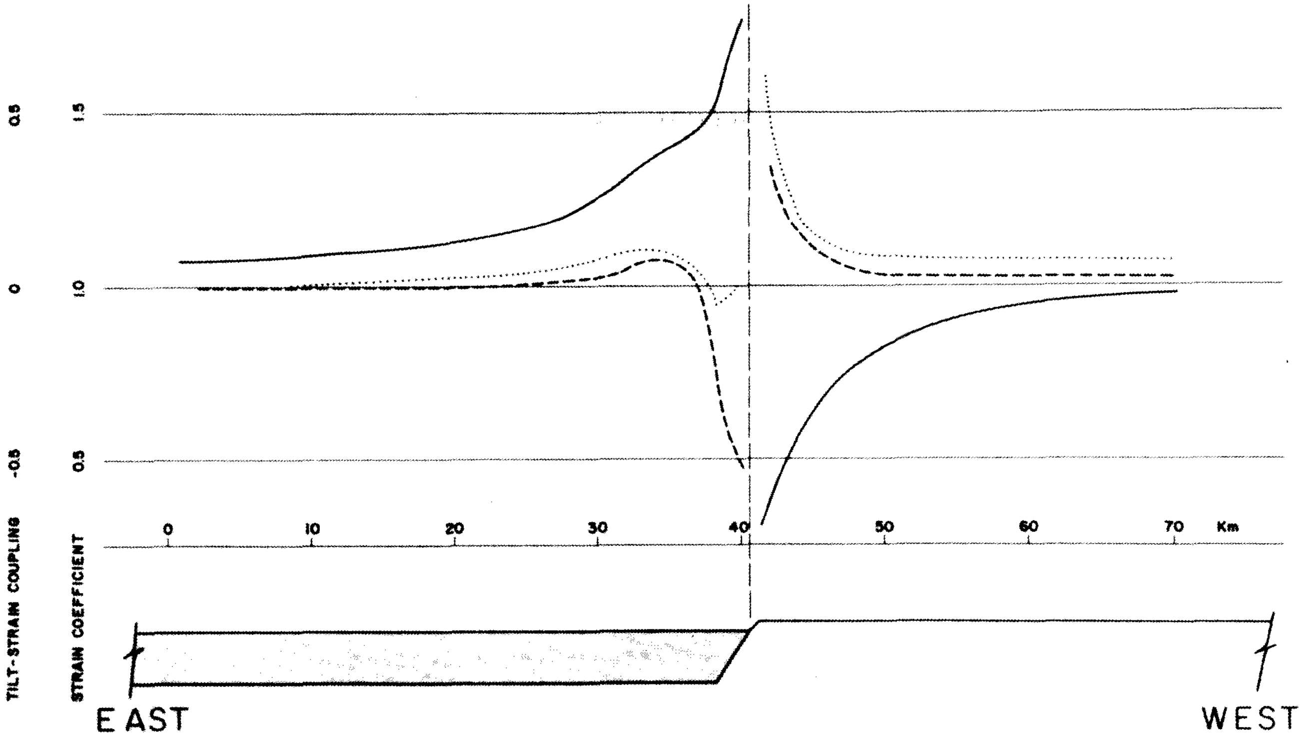

Fig. 2. Model used for two-dimensional finite element calculation of the influence of the Precambrian granite-to-sediment transition on surface strain (solid curve), horizontal tilt (dashed), and vertical tilt (dotted). The curve is reproduced from Harrison [1976].

an exactly N-S strike; the sediments were supposed to form a symmetrical basin about 40 sediment thicknesses in width (the assumption of symmetry allows the size of the computation to be halved and is reasonable because the strain perturbations are primarily an edge effect which becomes independent of basin width once the basin is many sediment thicknesses in width), and plane strain conditions were assumed. Stresses, which would have produced uniform strain in a homogeneous plate with a plane upper surface, were applied to the model and the actual surface strains computed with the ELAS finite element program [Utku, 1971]. The ratio of surface strain to that which would have been produced in the homogeneous material (the strain coefficient) is plotted in the figure. It is seen that the presence of the sediments reduces the E-W strain by about 50%. We have assumed that the shear strain is also reduced by 50% and that the N-S strain is unaffected by the boundary.

The next factor to be considered is the location of the strainmeter inside the Poorman Hill. The topography of this hill and its surroundings is shown in Figure 3; the strainmeter is at the marked spot, approximately 60 m below the ground surface and 1890 m above sea level. It can be seen that the instrument is above the surrounding topography on three sides; the sides of the hill are, of course, stress free, and this suggests that stress and strain observed at the Poorman site will be lower than the regional value.

In order to model this topographic effect, we considered a block of granite bounded by vertical sides at the positions of the edges of the map in Figure 3, extending to 1524 m below sea level and bounded by the actual surface topography on its upper surface. For computational purposes, this was subdivided into 405 elements arranged in five

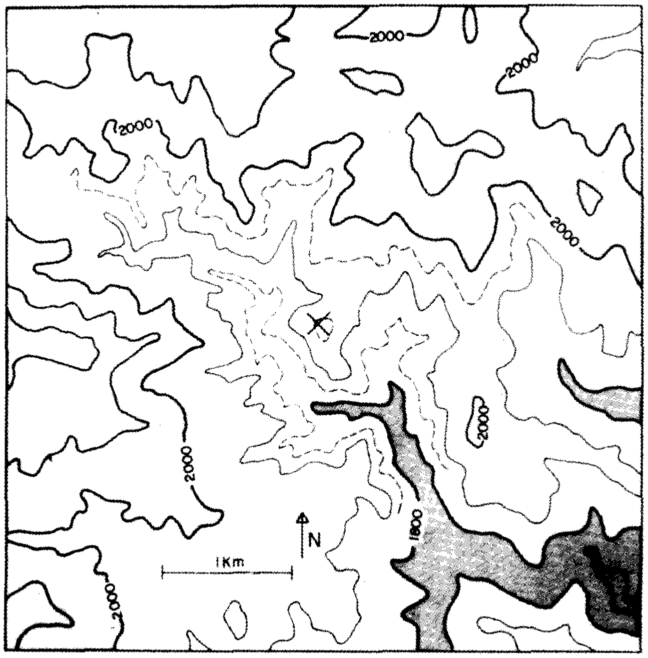

Fig. 3. Topography of area used in three-dimensional finite element computation of topographical influence on observed strain. Contour interval in 100 m (50-m contours dashed in the immediate vicinity of the Poorman Mine). Land above 2000 m and below 1800 m is shaded.

layers of 81 elements. The dimensions of the elements increased away from the observation site, so that a typical horizontal dimension was 60 m at the Poorman Hill itself and about 100 m near the margin of the block; topography was well represented within 600 m of the instrument site, but beyond this an increasing amount of smoothing by aliasing occurred, and no attempt was made to represent the topography along the outer margins of the block, a constant mean height being used instead. Three independent loads were applied to this model; in the absence of surface topography the first would have produced uniform N-S strain, the second uniform E-W strain, and the third uniform northeast shear strain. The SAPIV finite element computer program [Bathe et al., 1973] was then used to compute the actual strains at the strainmeter site inside the Poorman Hill for each of these loads. The 3 × 3 matrix of strain coupling coefficients is shown in Table 1.

The strainmeter [Levine and Hall, 1972] is located in a tunnel on an azimuth of 353° which can be regarded as straight over at least 60 m and has a diameter of about 2 m (Figure 4). If this cavity is modeled as an ellipsoid with 30:1 length to diameter ratio, then Harrison's [1976] Figure 3 shows that the strain magnification due to the cavity is less than 1%. The tunnel, however, takes a right angle bend near the end pier of the interferometer and is therefore more realistically modeled as a dead-ended tunnel. We have not taken into account the effect of the side tunnel which joins the interferometer tunnel at the approximate midpoint of the interferometer. The end pier is in fact 1½ tunnel diameters from the end wall, and Harrison's [1976] Figure 9b suggests that the strain magnification is of the order of 1½%.

The calculation was done in stages. First we calculated the body and load strain tides at the Poorman Mine; the E-W strain is reduced to 52.5% of its calculated value to take account of the Precambrian basement/sediment transition. These revised strains were then multiplied by the strain coupling factors of Table 1 to take account of the local topography. The computed strains were then rotated into the tunnel azimuth and multiplied by a factor of 1.015 to allow for magnification by the cavity. These results are summarized in Tables 2a and 2b.

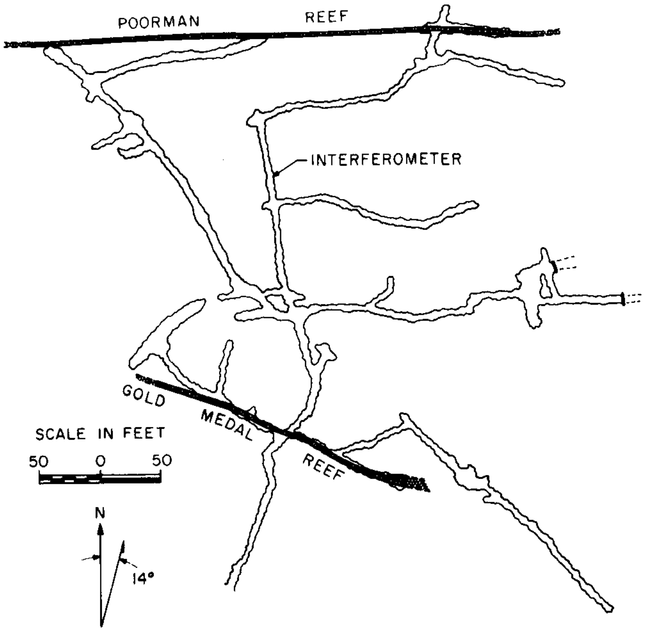

Fig. 4. Map of the Poorman Mine showing the location of the interferometer.

TABLE 1. Strain-Coupling Coefficients Relating Regional Strain to That at the Strainmeter Site

	Strain at Strainmeter Site		
Regional strain	N-S	E-W	NE shear
N-S	0.762	0.058	0.000
E-W	-0.047	0.785	-0.060
NE shear	-0.01	+0.046	0.670

The Instrument

The design of the strainmeter has been discussed in considerable detail [Levine and Hall, 1972; Levine and Stebbins, 1973]; only its general features will be mentioned here.

The heart of the strainmeter is an evacuated 30-m Fabry-Perot interferometer located along the length of the tunnel as shown in Figure 4. The interferometer is illuminated by a 3.39-μm helium-neon laser. A servo loop piezoelectrically tunes the laser to keep its wavelength coincident with one of the transmission maxima of the long interferometer. The frequency of the laser is therefore related to the length of the interferometer by $f = nc/2L$, where n is an integer, c is the velocity of light, and L is the length of the interferometer. Thus $\Delta f/f = -\Delta L/L$.

A second 3.39-μm laser is stabilized by using saturated absorption in methane [Levine and Hall, 1972]. The beat frequency between the two lasers is extracted for further processing. Thus

$$\frac{\Delta f_{\text{beat}}}{f} = \frac{\Delta L}{L}$$

or

$$\Delta f_{\text{beat}} = 8.85 \times 10^{13}\left(\frac{\Delta L}{L}\right)$$

The response of the strainmeter servo system is essentially flat from dc to 60 Hz. Not only is such bandwidth not necessary for tidal work, but its use substantially degrades subsequent processing by introducing an appreciable amount of servo noise.

We have used a combination of real time analog filtering and subsequent digital filtering to reduce the bandwidth to a more appropriate value.

The analog filter design represents a compromise between the need to attenuate high frequencies and the desire to minimize the phase shifts between the different tidal components. In addition it is vitally important not to introduce ripples in the passband of the transfer function. This latter requirement, coupled with the need to have filters which are simple to construct and

TABLE 2a. M_2 Strain Tide Computations in Parts in 10^9

	e_{NN}		e_{EE}		e_{NE}	
	Real	Imaginary	Real	Imaginary	Real	Imaginary
Body tide	12.56	0.	3.60	0.	0.	8.15
Ocean load	-1.09	-0.47	-0.53	-0.32	-1.83	-3.26
Sum tide*	11.47	-0.47	3.07	-0.32	-1.83	+4.89
E-W strain × 0.525, shear strain × 0.5 for regional geology	11.47	-0.47	1.61	-0.17	-0.91	+2.45
Multiply by coefficients of Table 1 for local topography	8.67	-0.37	1.74	-0.05	-0.71	+1.65

Body and load tide on 353° relative to body tide only: amplitude ratio is 0.932 and phase is -0.7°. Fully corrected tide on 353° relative to body tide only and including cavity magnification: amplitude ratio is 0.709 and phase is +0.9°.

*Load plus body.

whose transfer functions depend only weakly on component values, has forced us to consider only filters whose transfer characteristics are approximated by unity gain from dc to some frequency f_0, followed by a constant slope of 6n dB/octave above f_0.

The attenuation of such a filter at a high frequency is given by

$$T_h \cong 6n \log_2 \left(\frac{f_h}{f_0}\right) \text{dB} \qquad (1)$$

where $f_h > f_0$ while the phase shift at low frequencies is given by

$$\phi_\ell \cong n \frac{\Pi}{4}\left(\frac{f_\ell}{f_0}\right) \text{rad} \qquad (2)$$

where $f_\ell < f_0$. Thus the ratio T_h/ϕ_ℓ is independent of n. Since the noise spectrum is strongly peaked in the microseismic region (period of 6 s), there is no point in using n greater than unity. We then determine f_0 from (2) by requiring $\phi_\ell < 1/60$ rad when $f_\ell = 2$ cycles/day. We find $f_0 \sim 4$ cycles/h, which requires an RC product of approximately 100 s. We actually use a time constant of 80 s. The power spectral density of the earth noise transmitted by the filter is thus approximately

$$P(f) = 4 \times 10^{-22}\left(\frac{f_0}{f}\right)^4 (\Delta L/L)^2/\text{Hz}$$

for $f > f_0$ [Berger and Levine, 1974]. The total power transmitted from f_0 to ∞ is thus of order $4 \times 10^{-22}(\Delta L/L)^2$, which, if it were concentrated at frequency f_0, would imply an amplitude of about $3 \times 10^{-11}(\Delta L/L)$. This is less than 1% of the O_1 tidal amplitude, so that a recording system which sampled 10 times per hour would have negligible aliasing distortion. The incoherence between the broad band noise and the sampling clock reduces the effect even further. The analog output was digitized to 12 bits and recorded for further processing. The least significant bit of the digitizer corresponds to a strain of approximately $\Delta L/L = 7 \times 10^{-11}$.

The entire filtering and digitizing system was automatically calibrated in terms of a voltage standard 3 times per hour, and the voltage standard in turn was calibrated by using a standard cell and a precision potentiometer. Typical calibrations agreed to within ±0.1%.

TABLE 2b. O_1 Strain Tide Computations in Parts in 10^9

	e_{NN}		e_{EE}		e_{NE}	
	Real	Imaginary	Real	Imaginary	Real	Imaginary
Body tide	4.34	0.	6.93	0.	0.	-4.03
Load	0.28	-0.44	0.25	-0.05	+0.33	+0.22
Body plus load	4.62	-0.44	7.17	-0.05	+0.33	-3.80
E-W strain × 0.525 for regional geology	4.62	-0.44	3.77	-0.03	+0.16	-1.90
Multiply by coefficients of Table 1 for local topography	3.34	-0.32	3.24	-0.14	+0.12	-1.27

Body and load tide on 353° relative to body tide only: amplitude ratio is 1.046 and phase is -6.1°. Fully corrected tide on 353° relative to body tide only and including cavity magnification: amplitude ratio is 0.770 and phase is -9.1°.

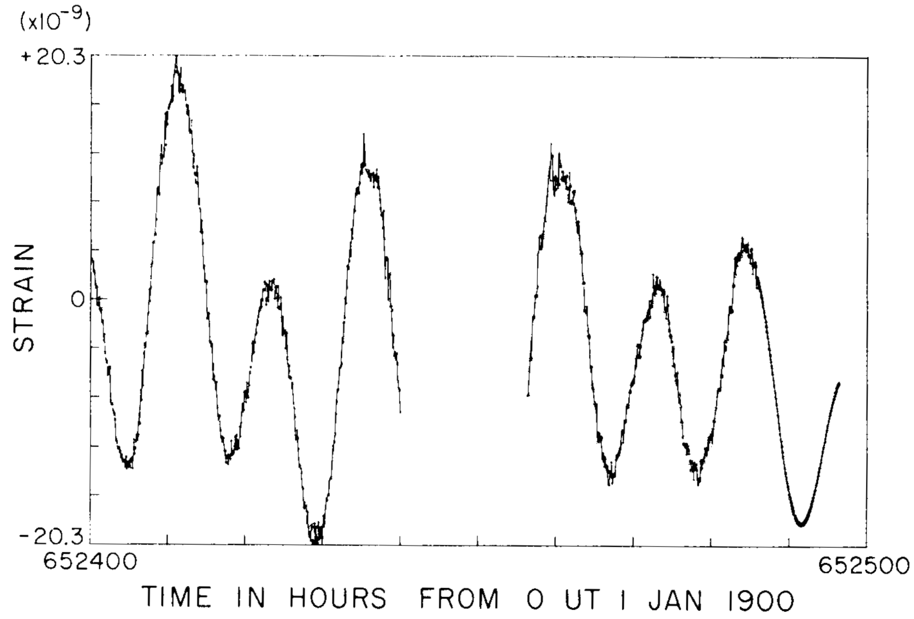

Fig. 5a. A break in the time series due to instrument malfunction.

Data Reduction

The first step in the analysis is to deal with the gaps due to instrumental failure. These gaps average about 10 h in length and occur approximately once per month. Because the gaps were so short, we chose to fill them rather than to perform our analysis on the various segments (individually or joined with zero fill). This permitted us to use our digital filter and other routines which require that the data be equally spaced in time.

To fill in the gaps in a way which minimizes the discontinuities in the data, we use a time series derived from a least squares analysis of the data immediately adjacent to the break. For example, consider a break in the data from time t_1 to time t_2. We expand the tidal potential in spherical harmonics:

$$V(t) = \sum_{n,m} a_{nm}(t) Y_{nm}(\theta, \phi) T_{nm} \qquad (3)$$

where Y_{nm} is the spherical harmonic at colatitude θ and longitude ϕ and a_{nm} are the time dependent parts of the potential. T_{nm} are adjustable constants adjusted so that V fits the

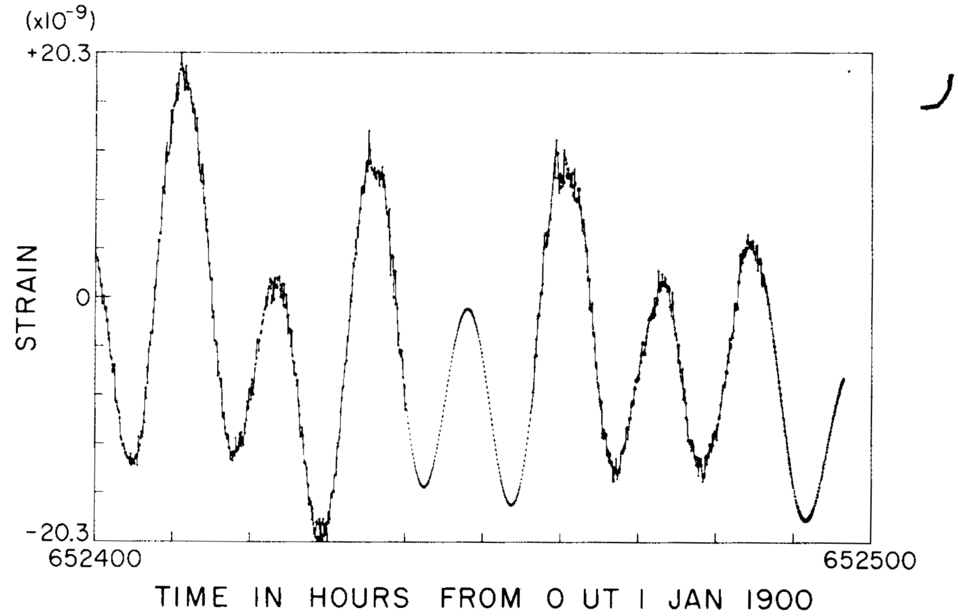

Fig. 5b. The same series as in Figure 5a with the break patched using the spherical harmonic expansion of the potential as discussed in the text. (Note that a second patch was made at the end of the time series.)

data from t_1 to $t_1 - \Delta_1$ and t_2 to $t_2 + \Delta_2$ in a least squares sense. We generally used a value of 7 days for Δ_1 and Δ_2. The values of T_{nm} are not sensitive to this choice. Occasionally (as in Figures 5a and 5b), two breaks occurred very close together. In this case the two breaks were fitted simultaneously by using data from before the first break and after the second. The values of T_{nm} determined in this way are then used to construct a time series from t_1 to t_2 by using (3). (A more detailed evaluation and justification for this expansion will be found below.)

We have tested this technique by using artificial gaps in our data. The fits to these 'gaps' were sufficiently close to the original time series that we were unable to identify the patched area in the residuals of the subsequent analysis.

A sample of the result of this fitting process is shown in Figures 5a and 5b. Figure 5a shows a typical data break. (In this case the break is in fact the first of two breaks approximately 24 h apart.) In Figure 5b we show the same data set with the patched time series inserted across the break. Note that in these and in all subsequent figures the data points are connected by straight lines for clarity. The symbol used at each point is chosen arbitrarily, different symbols being used solely to aid in identifying the graphs.

The full time series is then digitally bandpass filtered and decimated to one sample per hour. A typical digital filter response would have nominally unity gain across the tidal bands. It would have 3-dB points of 0.25 cycles/h and 0.02 cycles/h and would fall at about 40 dB/octave beyond these frequencies. All of the filters used are noncausal and have identically zero phase shift at all frequencies. The data are then truncated into consecutive 696-h segments for further analysis. This length is chosen to minimize contamination of the O_1 and M_2 components by nearby weaker lines, while at the same time retaining a sufficiently large number of blocks so as to make possible some estimate of the variance of the calculations. In addition this analysis technique allows us to discover any time dependence of the transfer function produced, for example, by changes in the local water table. Each segment is identified by its start time, measured in hours from 0 UT on January 1, 1900. The results presented here are based on an analysis of nine consecutive segments starting in March 1974.

Fourier transform analysis. The simplest way of analyzing the data is to perform a Fourier transform of the data at the frequencies appropriate for the O_1 and M_2 components (0.03873066 cycles/h and 0.0805114 cycles/h, respectively).

The amplitude and phase computed in this way are compared with the results obtained by computing the Fourier transform of a theoretical tidal series for the same time period. The theoretical tidal series is generated by using the technique proposed by *Munk and Cartwright* [1966] as modified by *Harrison* [1971] to compute the position of the moon by using Brown's theory.

Using this method, we obtain the following values for the transfer function:
$T(O_1) = 0.694 \pm 0.018$; $\Phi(O_1) = -15.9° \pm 5°$; $T(M_2) = 0.765 \pm 0.01$; and $\Phi(M_2) = -34° \pm 5°$, where T is the amplitude of the transfer function and Φ is the phase angle. A negative phase angle implies that the data lead the theory, i.e., that the peak of the local tide occurs before meridian passage. The quoted uncertainties represent the formal 1 standard deviation and do not include systematic errors.

The contamination of the estimate due to residual random noise is quite small. Using our published noise power spectral density [*Berger and Levine*, 1974] with an integration time of 696 h would suggest that the noise was of order $\Delta L/L \sim 3 \times 10^{-11}$ at a period of 12 h and of order $\Delta L/L \sim 10^{-10}$ at 24 h.

The amplitude signal-to-noise ratio is thus about 25 at O_1 and 400 at M_2. The observed standard deviations are consistent with these estimates.

Spherical harmonic expansion. We have also analyzed our data by using an expansion of the theoretical tidal signal in spherical harmonics.

We shall use the conventional spherical coordinate system with θ the colatitude and λ the longitude measured east from Greenwich. Then since we are near the surface of the earth, the strain along a particular horizontal direction which makes an angle θ_s (measured clockwise from north) with the meridian can be expanded in terms of the strains along the coordinate axes:

$$\varepsilon = \varepsilon_{\theta\theta} \cos^2 \theta_s + \varepsilon_{\lambda\lambda} \sin^2 \theta_s - \varepsilon_{\theta\lambda} \sin \theta_s \cos \theta_s \tag{3}$$

The strain tensor components are in turn related to the potential w:

$$\begin{aligned} \varepsilon_{\theta\theta} &= \frac{\ell}{gr} \frac{\partial^2 w}{\partial \theta^2} + \frac{hw}{gr} \\ \varepsilon_{\lambda\lambda} &= \frac{\ell}{gr \sin^2 \theta} \frac{\partial^2 w}{\partial \lambda^2} + \frac{\ell}{gr} \cot \theta \frac{\partial w}{\partial \theta} + \frac{h}{gr} w \qquad (4) \\ \varepsilon_{\theta\lambda} &= \hat{i} \frac{2\ell}{gr \sin \theta} \left\{ \frac{\partial^2 w}{\partial \theta \partial \lambda} - \cot \theta \frac{\partial w}{\partial \lambda} \right\} \end{aligned}$$

where h and ℓ are Love's numbers, g is the local acceleration of gravity, r is the radius of the earth, w is the driving potential in units of centimeters of equilibrium height, and $\hat{i} = (-1)^{1/2}$.

We may expand the driving potential in terms of a time dependent term $c_n^m(t)$ and an angular term involving only the station coordinates:

$$w(\theta, \lambda, t) = \sum_{m,n} c_n^m(t) Y_n^m(\theta, \lambda) \tag{5}$$

where Y_n^m is the normalized spherical harmonic.

If we substitute (5) into (4) and use these results in (3), we find that the strain can be expanded into spherical harmonics

$$\varepsilon(\theta_s, \theta, \lambda, t) = \sum_{m,n} \xi(m, n) c_n^m(t) \tag{6}$$

where $c_n^m(t)$ is the time dependent component of the potential having (n, m) symmetry on the earth's surface. The quantities $\xi(n, m)$ are given in the appendix for various values of n and m.

Equation (6) gives the strain that would be observed on a theoretical strainmeter. We hypothesize that our instrument and site have some transfer function T_{nm} which depends on n and m but not on t. Then the observed strain signal is of the form

$$\varepsilon(t) = \sum_{m,n} T_{nm} c_n^m(t)\xi(m, n) \qquad (7)$$

To evaluate T_{nm}, we construct the quantities

$$\varepsilon(n, m, t) = T_{nm} c_n^m(t)\xi(m, n)$$

and adjust the various T_{nm} so that (7) is a best fit to our data in a least squares sense.

In the current discussion we are interested in the M_2 and O_1 components. These components obviously have m = 2 and m = 1 symmetries, respectively. The significant T matrix elements are thus T_{21} and T_{22}. We have obtained the following values for these components: $T_{21} = 0.633 \pm 0.02$, $\Phi_{21} = -9° \pm 5°$, $T_{22} = 0.722 \pm 0.04$, and $\Phi_{22} = -29° \pm 6°$, where Φ_{nm} is the phase angle of the associated T_{nm}. Note that the transfer functions obtained in this analysis are not for a given frequency component but for a given symmetry.

Discussion of Results

Table 3 summarizes the results of our analysis. These results should be compared with the summary of the calculations in Table 2.

Unfortunately, both the Fourier transform method and the spherical harmonic method produce estimates of the transfer function which may be biased.

Using the Fourier transform method with conventional boxcar apodization results in the convolution of the spectral estimates with

$$\sin(\pi fT)/(\pi fT)$$

where T is the record length. Thus the estimate of the O_1 amplitude is contaminated by approximately 8% of the P_1, K_1, S_1 estimate. (The P_1, K_1, and S_1 components are not resolved with a record length of 696 h. However, most of the power comes from K_1, and it is the dominant contaminant.) This bias is not removed by computing the ratio of the spectral estimate of the data to the spectral estimate of the theory unless the O_1 and P_1, K_1, S_1 transfer functions are the same. Our analysis suggests that either the P_1, K_1, S_1 transfer function is significantly smaller (by about 20%) than the O_1 transfer function or the load contribution is significantly different. Thus the O_1 spectral estimate should be biased by about 1.6%. Furthermore, the estimate of the P_1, K_1, S_1 amplitude varies from month to month, since the three components beat against each other. This will appear as an apparent variation in the amplitude of the spectral estimate and an apparent fluctuation in the phase of approximately ±1°. A problem of smaller proportions exists for M_2.

We conclude that perhaps 50% of the standard deviation associated with the O_1 Fourier transform amplitude estimate arises from this source. The effect is smaller for M_2 and accounts for approximately 20% of the measured standard deviation of the amplitude estimate.

The spherical harmonic analysis is subject to a different set of problems. The most serious problem from the point of view of the current discussion is that the transfer function is computed by symmetry group rather than by frequency. This procedure implicitly assumes that all of the diurnal frequencies have the same effective transfer function relative to the local tidal potential. As mentioned previously, this assumption is not correct, at least for the diurnal components, for the data that we have analyzed here. This limitation can be overcome by modifying (7) to allow for leads or lags. Thus (7) is replaced by

$$\varepsilon(t) = \sum_{\Delta} \sum_{m,n} T_{n,m}(\Delta) c_n^m(t \pm \Delta)\xi(m, n) \qquad (8)$$

This allows the transfer function to be different for different components of the same symmetry. The frequency dependent transfer function z(f) is then related to $T_{nm}(\Delta)$ by

TABLE 3. Results of the Data Analysis

		Transfer Function	
Tidal component	Method of analysis	Amplitude	Phase
Diurnal O_1	Fourier transform, 696 h	0.694 ± 0.018	-15.9° ± 5°
Diurnal O_1	Long transform, 2784 h	0.710	-18°
Semidiurnal M_2	Fourier transform	0.765 ± 0.01	-34° ± 5°
Semidiurnal M_2	Long transform	0.753	-29°
Diurnal (n = 2, m = 1)	Spherical harmonics	0.633 ± 0.02	-09° ± 5°
Diurnal O_1	Lead/Lag	0.685 ± 0.02	-10° ± 5°
Semidiurnal (n = 2, m = 2)	Spherical harmonics	0.722 ± 0.04	-29° ± 6°
Semidiurnal M_2	Lead/Lag	0.710 ± 0.04	-28° ± 6°
Average O_1		0.696 ± 0.02	-15° ± 5°
Theory O_1		0.770	-09.1°
Average M_2		0.743	-30° ± 5°
Theory M_2		0.709	+0.9°

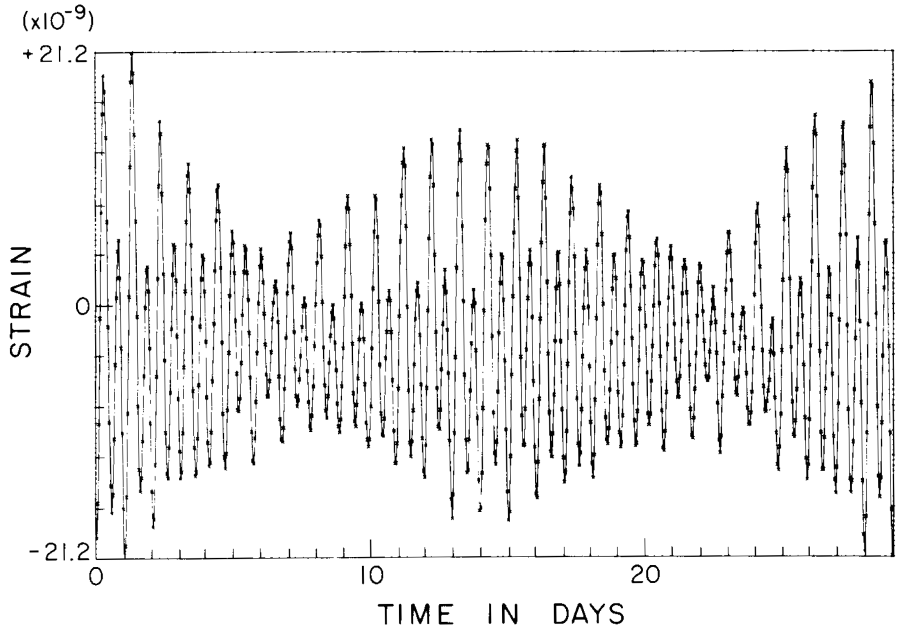

Fig. 6. Band-pass filtered time series for data set 652763.9.

$$z(f) = \sum_{\Delta} \sum_{n,m} T_{nm}(\Delta) \exp(-i\pi f\Delta/288)$$

where f is in cycles per hour and Δ is in hours. We have repeated our analysis by using seven values of Δ: -72 h, -48 h, -24 h, 0 h, +24 h, +48 h, and +72 h. The rms residuals (computed by taking the rms of the difference between the data and the time series as computed from (8)) are about 2% of the amplitude of the data. In contrast, when (7) is used to fit the data, the rms residuals are of order 3½%.

The values of the transfer function computed in this manner for the O_1 and M_2 components are also shown in Table 3 under analysis method lead/lag. Note that in general the lead/lag analysis tends to bring the transfer functions computed by the two methods into closer agreement and that the discrepancies are within the quoted uncertainties.

In addition to the numerical problems discussed above, we have some evidence that the assumption of a simple linear relationship between applied potential and measured strain, which underlies all of our analysis, is only approximately true. This can be most clearly illustrated by considering data set 652763.9 (data sets are identified by their starting time measured in hours from 0 UT, January 1, 1900).

Figure 6 shows the time series after it has been band-pass filtered and decimated to one sample per hour. The Fourier transform of the data set is shown in Figure 7. Note that the semidiurnal amplitudes sit on a rather broad pedestal. This can be seen much more clearly by examining the residual time series obtained by

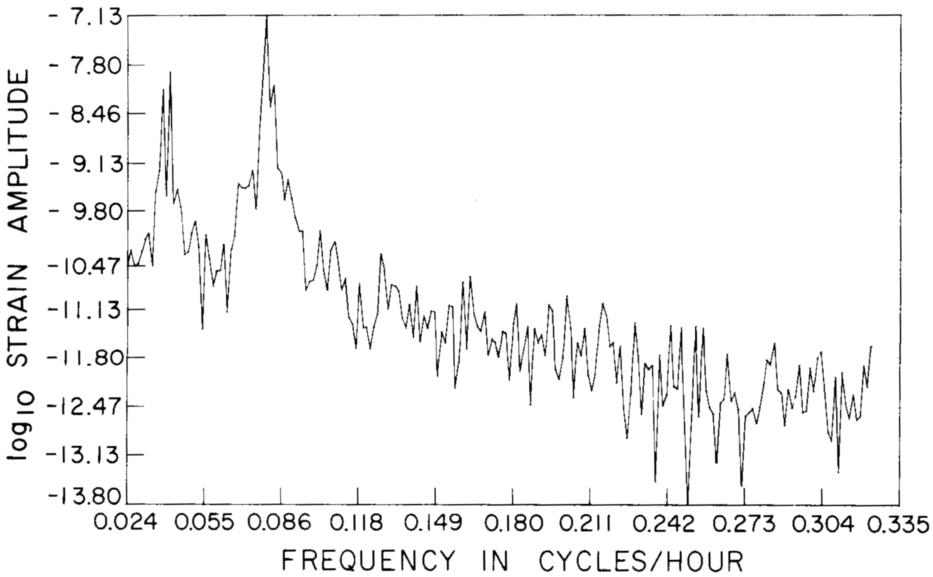

Fig. 7. Fourier transform of the data shown in Figure 6.

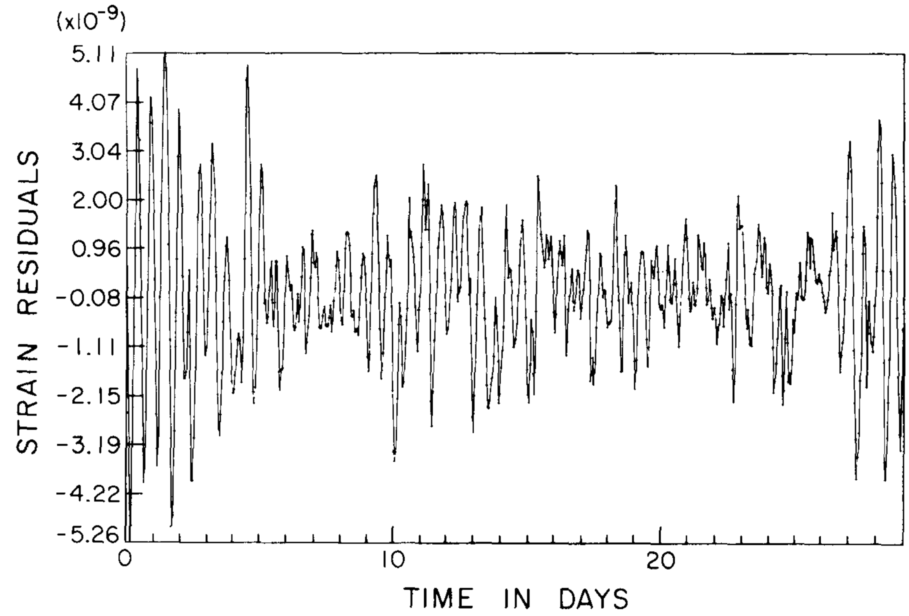

Fig. 8. Residuals of a least squares fit of the data using a spherical harmonic expansion of the potential.

subtracting the theoretical tides as determined by the spherical harmonic expansion method described above.

The residual time series is shown in Figure 8, and its Fourier transform is shown in Figure 9. Two points are worth noting. (1) The residuals tend to be proportionally larger when the tides are large than when they are small. (2) The Fourier spectrum shows that most of this power is concentrated near the semidiurnal tidal peak but that it is a continuous rather than a strongly peaked distribution.

An hypothesis which we have considered in trying to explain these facts is that the system responds nonlinearly to the applied strain. (By system we mean to include local geology, the interferometer and its piers, and all the subsequent electronics.) To test this hypothesis, we have constructed time series of the form $C_{nm}(t) \cdot C_{n'm'}(t)$ and have repeated the least squares analysis by using several quadratic terms of this form in the potential. In Figure 10 we show the residual time series after these quadratic terms have been removed, and in Figure 11 we show the Fourier transform of the residuals. Not only have the residuals been reduced in amplitude, but their character is changed as well. The broad semidiurnal power peak has been removed by the fit. In addition, both the spectrum of Figure 11 and a statistical analysis of the data of Figure 10 show that the residual time series can be approximated by passing white noise through the band-pass filter used to filter the data. This implies that most of the residuals of the nonlinear fit are noise.

In fact the residual amplitude can be reduced slightly further by fitting time series of the form $B(t) \cdot C_{nm}(t)$, where $B(t)$ is the local baro-

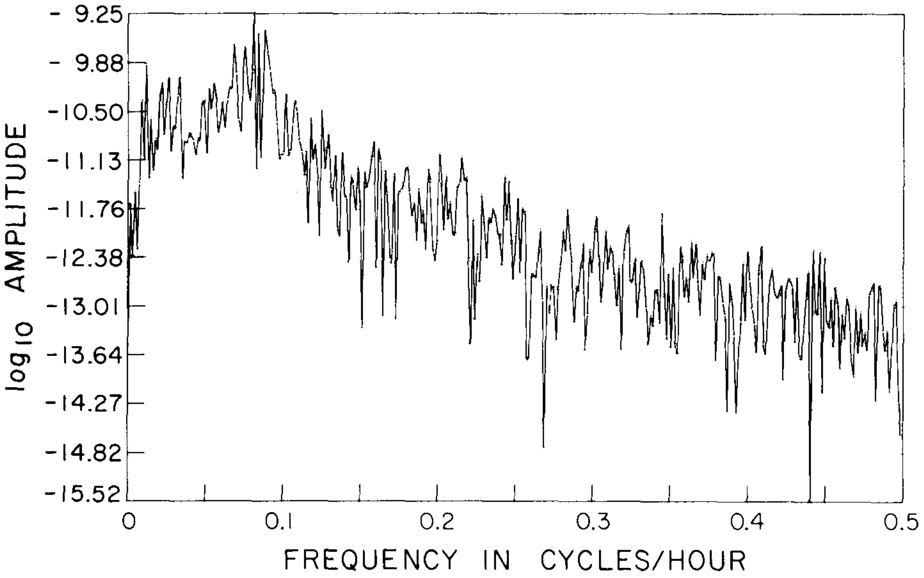

Fig. 9. Fourier transform of the residuals shown in Figure 8.

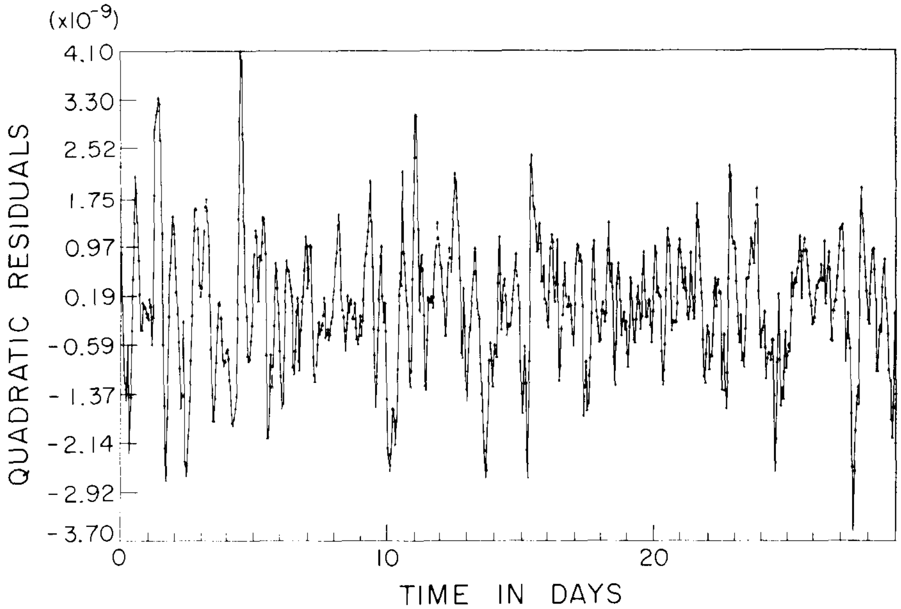

Fig. 10. Residuals of a least squares fit of the time series shown in Figure 8 using products of spherical harmonics.

metric pressure. The reduction is small (about 15%) but statistically significant.

These reductions in the residuals are not merely numerical accidents obtained by fitting a series of roughly the right spectral density. We have used many other combinations of series which, although they have roughly the same power spectra, show no coherence with the data whatsoever. Thus local air temperature, local rock temperature, and local solar radiation do not reduce the variance in a statistically significant way (fractional reduction of 0.01% or less) when they are used either in a linear or quadratic analysis, in spite of the fact that their power spectra are all roughly alike. We are forced to conclude that the nonlinear fit produces statistically significant reductions in the variance of the residuals and that the reduction in the variance obtained by using terms quadratic in the applied potential cannot be matched by any other linear or quadratic term that we have tried.

We have not found a reason for the presence of the quadratic terms that we have used. We have eliminated the entire instrument with the exception of the piers by calibration in terms of frequency or voltage standards. We are left with three possibilities: (1) the piers, (2) the mine, and (3) deficiencies in the tidal theory.

We have applied some calibration signals to the piers. We have not been able to observe any significant nonlinearity, but our tests are by no means conclusive.

We have not been able to construct a theory of the mine tunnels that agrees with the observations, but in view of the complexity of the local geology this remains a real possibility.

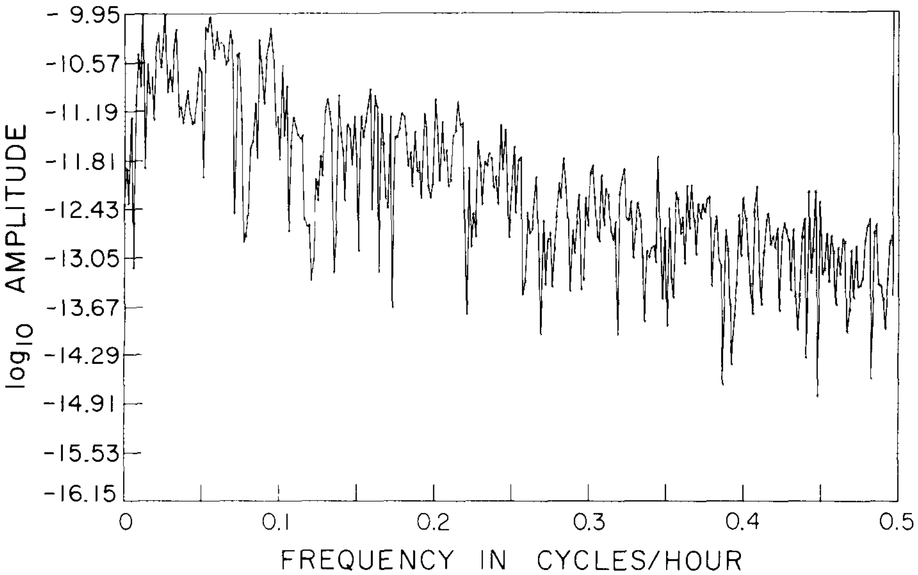

Fig. 11. Fourier transform of the residuals shown in Figure 10.

There is some additional evidence that conventional tidal theory may be deficient when it is applied to local strain. If we analyze the data in 4-month (2784 h) blocks instead of 1-month (696 h) blocks, we obtain slightly different values for the transfer functions (Table 3, Long transform) which are just barely inside the quoted error bars for the shorter transforms. Furthermore, the rms amplitude of the residuals following a spherical harmonic analysis is noticeably poorer for the long series than for any of the component shorter ones (almost 6% versus an average of about 3½%) even if terms having n = 3 symmetry are added to the fit. This suggests that tidal theory might not adequately predict long-period terms. However, this same effect could also be produced by a time variation of the local effects.

We have also analyzed our data in longer lengths by using series lengths from 5 months up to the full 9 months at once. The transfer functions obtained in this way agree with the shorter transforms to within the quoted uncertainties. However, we do not have enough data at the moment to estimate the variance in these estimates, since the number of blocks is too small.

There is a major difficulty with assuming that nonlinear effects are present which suggests that the problem is more complicated than simple models would indicate. It is difficult to construct a simple nonlinear theory which does not produce a significant spectral peak near 4 cycles/day (twice the M_2 frequency). As can be seen from any of the Fourier spectra (e.g., Figure 9), such a peak is very weak if it exists at all.

In view of the complexity of the local geology, we feel that the existence of nonlinearities in the earth tide response cannot be confirmed from our data. Indeed, some form of time variability in the transfer function from regional strain to local strain or some azimuthal dependence of the transfer function due to the asymmetric fracture distribution in the nearby rock is the most likely source of our observed effect. But we are unable to construct any quantitative model which adequately accounts for our large residuals and substantial fluctuations in the phase of the linear transfer functions. In addition the large residual phase discrepancy at M_2 remains unexplained.

We have considered time variations in the local hydrology as a source of slow changes in the transfer functions which might broaden the peaks in the observed spectrum. However, the transfer functions do not seem to differ significantly from summer to winter in spite of the large seasonal variations in the level of the groundwater.

The Fourier transform of the data (Figure 7) is suggestive of 'tidal cusping' which has been observed in ocean tides [Munk and Cartwright, 1966] measured at ports located on relatively shallow continental shelves. However, since neither effect has, to our knowledge, been quantitatively explained, it is difficult to decide if this is simply coincidental or if it implies a more general problem in tidal analyses.

At the bottom of Table 3 we show a comparison between the transfer functions predicted by a linear theory modified by local topography and crustal inhomogeneities and an analysis of the data. In view of the many simplifying assumptions of the model the agreement between theory and experiment is good. The residual discrepancy in the O_1 amplitude is about 10%, while the M_2 amplitude discrepancy is about 3%. The phase angle discrepancies have been reduced from -15° to -9° for O_1 and from -30° to -23° for M_2.

Conclusions

We have shown that by considering local topography and local crustal inhomogeneities, the agreement between strain tide theory and experiment can be substantially improved. There appear to be residual systematic differences which are not yet understood and which may be modeled as small nonlinearities in the local geology or in the global properties of the earth. Approximately 99% of the variance of the initial time series can be predicted by using a sum of linear and quadratic terms in the potential. The residual variance has a distribution consistent with the hypothesis that it is band-passed white noise.

Alternatively, the differences may have their origins in deficiencies in classical tidal theory or in its application to sites with local crustal inhomogeneities.

Appendix: Spherical Harmonic Expansion Coefficients

We present here the coefficients of the various terms in the spherical harmonic expansion of the potential defined in (6). The quantities are as defined above in connection with (4), (5), and (6):

$$\xi(2,\ 0) = \frac{1}{gr}\left(h - \frac{6\ell\cos 2\theta}{3\cos^2\theta - 1}\right)\cos^2\theta_s +$$

$$\frac{1}{gr}\left(h - \frac{6\ell\cos^2\theta}{3\cos^2\theta - 1}\right)\sin^2\theta_s$$

$$\xi(2,\ 1) = \frac{1}{gr}(h - 4\ell)\cos^2\theta_s +$$

$$\frac{1}{gr}\left(h - \frac{\ell}{\sin^2\theta} + 2\ell\cot\theta\cot 2\theta\right)\sin^2\theta_s -$$

$$\hat{i}\,\frac{1}{gr}\,\frac{2\ell}{\sin\theta}\,(2\cot 2\theta - \cot\theta)\sin\theta_s\cos\theta_s$$

$$\xi(2,\ 2) = \frac{1}{gr}\left[h + 2\ell(\cot^2\theta - 1)\right]\cos^2\theta_s$$

$$+\frac{1}{gr}\left(h - \frac{4\ell}{\sin^2\theta} + 2\ell\cot^2\theta\right)\sin^2\theta_s$$

$$+\,\hat{i}\,\frac{1}{gr}\left(\frac{4\ell\cot\theta}{\sin\theta}\right)\sin\theta_s\cos\theta_s$$

$$\xi(3,\ 0) = \frac{1}{gr}\left\{h + \ell\left[\frac{3(11 - 15\cos^2\theta)}{5\cos^2\theta - 3}\right]\right\}\cos^2\theta_s$$

$$+\frac{1}{gr}\left[h - \ell\left(1 + \frac{10\cos^2\theta}{5\cos^2\theta - 3}\right)\right]\sin^2\theta_s$$

$$\xi(3, 1) = \frac{1}{gr}\left\{h - \ell\left[1 + \frac{10(1 - 4\cos^2\theta)}{1 - 5\cos^2\theta}\right]\right\}\cos^2\theta_s$$

$$+ \frac{1}{gr}\left[h + \ell\left(\cot^2\theta - \frac{1}{\sin^2\theta} - \frac{10\cos^2\theta}{5\cos^2\theta - 1}\right)\right]$$

$$\times \sin^2\theta_s - \hat{i}\,\frac{1}{gr}\left(-\frac{20\ell\cos\theta}{5\cos^2\theta - 1}\right)\cos\theta_s\sin\theta_s$$

$$\xi(3, 2) = \frac{1}{gr}\left[h + \ell(2\cot^2\theta - 7)\right]\cos^2\theta_s$$

$$+ \frac{1}{gr}\left[h + \ell\left(2\cot^2\theta - 1 - \frac{4}{\sin^2\theta}\right)\right]\sin^2\theta_s$$

$$- \hat{i}\,\frac{1}{gr}\left[\frac{4\ell(\cot\theta - \tan\theta)}{\sin\theta}\right]\sin\theta_s\cos\theta_s$$

$$\xi(3, 3) = \frac{1}{gr}\left[h + \ell(6\cot^2\theta - 3)\right]\cos^2\theta_s$$

$$+ \frac{1}{gr}\left[h + \ell\left(3\cot^2\theta - \frac{9}{\sin^2\theta}\right)\right]\sin^2\theta_s$$

$$+ \hat{i}\,\frac{1}{gr}\left(\frac{12\ell\cot\theta}{\sin\theta}\right)\sin\theta_s\cos\theta_s$$

Acknowledgment. This work was supported in part by the National Science Foundation under grant GA-36365 through the University of Colorado.

References

Bathe, K.-J., E. L. Wilson, and F. E. Peterson, SAPIV, a structural analysis program for static and dynamic response of linear systems, Rep. EERC 73-11, Earthquake Eng. Res. Center, Coll. of Eng., Univ. of Calif., Berkeley, Calif., 1973.

Berger, J., and J. Levine, The spectrum of earth strain from 10^{-8} to 10^{+2} Hz, J. Geophys. Res., 79, 1210-1214, 1974.

Erickson, E. L., D. E. Miller, and K. H. Waters, Shear-wave recording using continuous signal methods, 2, Later experimentation, Geophysics, 33, 240-254, 1968.

Farrell, W. E., Deformation of the earth by surface loads, Rev. Geophys. Space Phys., 10, 761-797, 1972a.

Farrell, W. E., Global calculations of tidal loading, Nature, 238, 43, 1972b.

Harrison, J. C., New computer programs for the calculation of earth tides, report, Coop. Inst. for Res. in Environ. Sci., Univ. of Colo., Boulder, 1971.

Harrison, J. C., Cavity and topographic effects in tilt and strain measurement, J. Geophys. Res., 81, in press, 1976.

Healy, J. H., W. H. Jackson, and J. R. Van Schaack, Geophysical and geological investigations relating to earthquakes in the Denver area, Colorado, 5, open file report, U. S. Geol. Surv., Washington, D. C., 1966.

Hendershott, M. C., and W. H. Munk, Tides, Annu. Rev. Fluid Mech., 2, 205-224, 1970.

Humphrey, A. G., Jr., The geology of Poorman Hill and the Poorman Mine, Boulder County, Colorado, M.S. thesis, Univ. of Colo., Boulder, 1955.

Levine, J., and J. L. Hall, Design and operation of a methane absorption stabilized laser strainmeter, J. Geophys. Res., 77, 2595-2609, 1972.

Levine, J., and R. T. Stebbins, Ultra sensitive laser interferometers and their application to problems of geophysical interest, Phil. Trans. Roy. Soc. London, Ser. A, A274, 279-284, 1973.

Munk, W. H., and D. E. Cartwright, Tidal spectroscopy and prediction, Proc. Roy. Soc. London, Ser. A, A259, 533-581, 1966.

Munk, W. H., F. Snodgrass, and M. Wimbush, Tides offshore: Transition from California coastal to deep sea waters, Geophys. Fluid Dyn., 1, 161-235, 1970.

Tiron, K. D., Y. Sergeev, and A. Michurin, Tidal charts for the Pacific, Atlantic and Indian oceans, Engl. Transl., Vestn. Leningrad Univ., Geol. Geogr., 24, 123-137, 1967.

Utku, S., ELAS75 computer program for linear equilibrium problems of structures, Users Manual, Struct. Mech. Ser., no. 10, Department of Civil Engineering, Duke University, Durham, N. C., 1971.

(Received April 2, 1975;
revised October 17, 1975;
accepted November 4, 1975.)